PHYSICS

THz induced giant spin and valley currents

Sangeeta Sharma*, Peter Elliott, Samuel Shallcross*

Spin and valley indices represent the key quantum labels of quasi-particles in a wide class of two-dimensional materials and form the foundational elements of the fields of spintronics and valleytronics. Control over these degrees of freedom, therefore, remains the central challenge in these fields. Here, we show that femtosecond laser light combining optical frequency circularly polarized pulse and a terahertz (THz) frequency linearly polarized pulse, a so-called "hencomb" pulse, can generate precisely tailored and 90% pure spin currents for the dichalcogenide WSe_2 and >75% pure valley currents for bilayer graphene with gaps greater than 120 millielectron volts (dephasing time, 20 femtoseconds). The frequency of the circular light component and the polarization vector of the THz light component are shown to represent the key control parameters of these pulses. Our results thus open a route toward light control over spin/valley current states at ultrafast times.

INTRODUCTION

Two-dimensional (2D) materials with broken inversion symmetry may host quasi-particles that, in addition to the fundamental spin and charge of the electron, have a remarkable additional degree of freedom: valley pseudo-spin (*1*–*3*). This denotes which of the degenerate but nonequivalent low-energy band manifolds the quasi-particle is located at within the first Brillouin zone and, crucially, it is possible to optically address this degree of freedom. Using carefully tailored light pulses, one may selectively generate excitons or single-particle charge carriers at a particular valley (*4*–*11*), opening the way to use the valley as a "quantum bit." Both spin- and valleytronics offer many potential advantages over classical electronics in terms of data manipulation velocity and energy efficiency (*12*). However, while spin excitations suffer from a dynamical loss of character arising from the spin-orbit (SO)–induced spin precession, the valley wave function represents a "data bit" whose stability is threatened only by intervalley scattering, a feature controllable by sample quality. Valleytronics thus presents a potentially robust platform for going beyond classical electronics. At the heart of any future, valleytronics or spintronics technologies will, in addition to quantum excitations encoding data bits, reside the control and creation of valley and spin currents. However, while sustained attention has been paid to the task of tailoring lightforms on ultrafast time scales to selectively excite valley quasi-particles, the precise creation and control of valley and spin currents by femtosecond laser pulses remain less developed (*13*, *14*).

Early attempts at generating pure spin and valley currents focused on nonoptical generation via the spin Hall effect; however, the small spin Hall angles of many materials frustrated these efforts. Subsequent experiments have demonstrated the possibility to use circularly polarized light in a gated hall bar geometry to generate spin current in WSe_2 (*15*), imaged valley currents in WS_2-WSe_2 heterostructures (*16*), and used the valley Hall effect in creating valley current (*17*). However, in graphene and few-layer graphenes, ideal spin-, and valleytronics materials due to their long-scattering lengths, generation of bulk pure valley current remains a sought goal.

Here, we wish to show that, by tailoring light pulses that combine terahertz (THz) and optical light, one can achieve complete control over valley current in a wide range of valley active materials. We demonstrate the generation of 90% pure spin currents in the representative strong SO-coupling dichalcogenide WSe_2 and, in addition, show that the same pulse generates a >75% pure valley current in bilayer graphene with gaps greater than 120 meV (dephasing time 20 fs).

As THz light has energies comparable to key electronic features, for example, typical superconducting gaps and magnetization energy differences, it has come under increasing attention both as a spectroscopic probe and a means of control in quantum materials (*7*, *18*–*22*). Here, we show that modulating femtosecond pulses of circularly polarized light with a linearly polarized THz envelope allows the creation of a precisely controllable valley photocurrent, a notable example of THz control over electronic properties. We first establish our results using a minimal tight-binding model for the dichalcogenide WSe_2 and bilayer graphene, before using state-of-the-art time-dependent density functional theory (TD-DFT) simulations to confirm the effect in realistic material simulations.

RESULTS

Hencomb pulse

Spin-valley locking has its origin in the valley-selective response to circularly polarized light. This can be viewed, in the case of 2H structure dichalcogenides such as WSe_2, as arising from a selection rule involving the magnetic quantum numbers of the *d*-orbitals that comprise the gap edge states. While circularly polarized light excites valley charge, it does not, however, create a valley current. Using a minimal four-band description to describe the low-energy bands of WSe_2, we show in Fig. 1 (A to D) this result; details of the Hamiltonian, pulse construction, and time propagation can be found in Materials and Methods. In Fig. 1A, we display the vector potential of the circularly pulse which, as shown in Fig. 1B, excites charge only (in this case) at the *K* valley. This charge excitation results, however, in no valley current (Fig. 1D) for the reason that, for

Max-Born-Institut für Nichtlineare Optik und Kurzzeitspektroskopie, Max-Born-Strasse 2A, 12489 Berlin, Germany.
*Corresponding author. Email: sharma@mbi-berlin.de (S.Shar.); shallcross@mbi-berlin.de (S.Shal.)

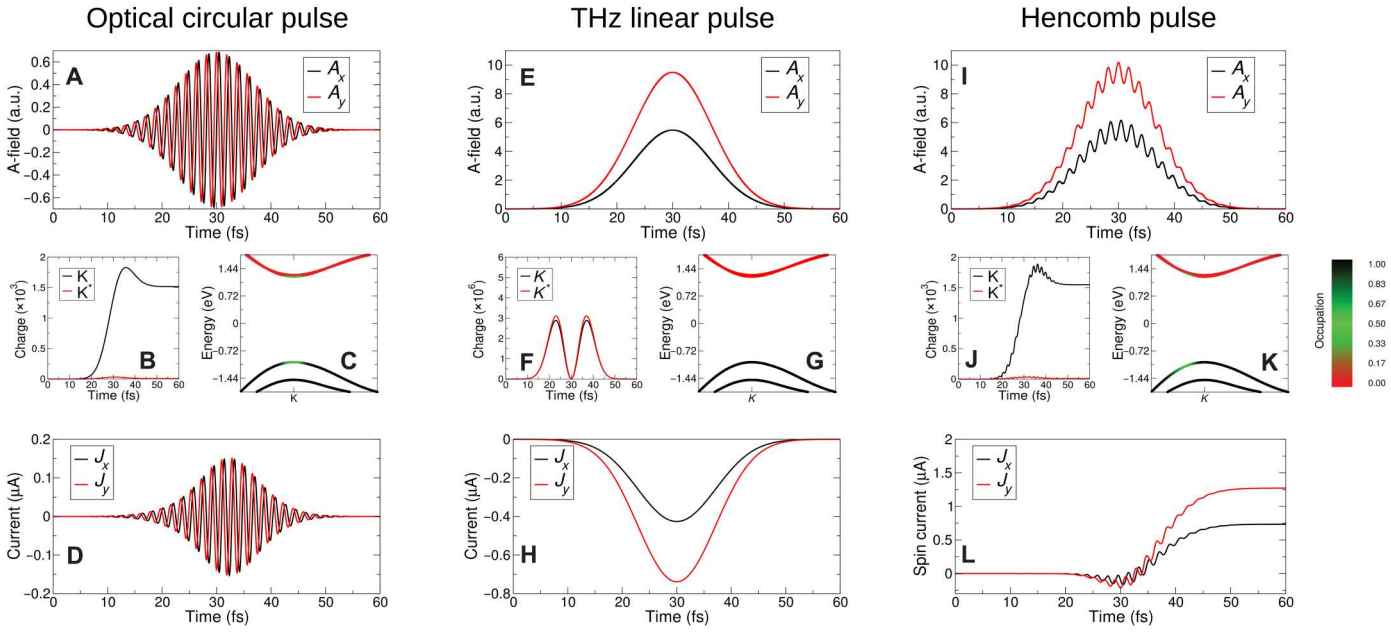

Fig. 1. Three distinct laser pulses applied to WSe_2: Circularly polarized, linearly polarized single-cycle THz, and a hencomb pulse. The corresponding vector potentials are shown in the first row; the vector potential amplitudes are 0.685 and 10.96 atomic units (a.u.) for the circular and THz pulse, respectively, with the frequency of the former 2.2 eV, just below the gap of 2.25 eV. While the circularly polarized pulse (**A**) excites valley-selected charge (**B** and **C**), where *K* and *K** refer to the charge excited at the conjugate valleys, it results in no net valley current (**D**), a fact which follows from the exact cancelation of current carrying states as illustrated in (C). The THz pulse, by contrast, generates neither excited charge nor a net valley current (**E** to **H**). Combining these two pulses, the hencomb pulse (**I** to **L**) breaks local valley inversion symmetry (K), resulting in a current carrying valley excitation and a residual spin current as shown in (L). The peak electric fields are 2.8 and 1.1 MV/cm for the optical and THz pulse components, respectively, with the peak power densities of 5.8×10^9 and 3.0×10^5 W/cm^2. In each case, the full width at half maximum (FWHM) is 16.5 fs.

each quasi-momentum in the valley k_{valley} that is excited, a corresponding $-k_{\text{valley}}$ also is excited: The Bloch velocities thus cancel and there is no net valley current. This can be seen in Fig. 1C in which the color of the band line represents occupation.

To create a valley excited state that does result in a net valley and spin current, the k_{valley} and $-k_{\text{valley}}$ degeneracy must be broken. As the laser vector potential couples directly to crystal quasi-momentum, $k \rightarrow k - \mathrm{A}(t)/c$, the most effective way in which this can be done is through a linearly polarized single-cycle pulse with duration comparable to that of the circularly polarized pulse: Such a pulse will evidently be in the "THz window" of 1 to 50 THz. This THz pulse is shown in Fig. 1 (E to H); the polarization vector is chosen to lie along the zigzag direction (an angle of 60°). Evidently, this pulse generates neither charge excitation nor a residual current. However, in combination with the circularly polarized pulse, a "hencomb" pulse (Fig. 1I), we find both valley-selective charge excitation and valley-selective current (Fig. 1, J and K, respectively). This results from a noncancelation of the Bloch velocities of excited quasi-momentum, as the distribution of excited charge is now shifted off the high-symmetry *K* point by exactly the polarization vector of the THz pulse.

The physical picture underpinning the action of this pulse is schematically illustrated in Fig. 2A: A half cycle of the THz component of the hencomb pulse drives an intraband motion sending states distant from the gap edge to the gap edge (i). At this point, the circularly polarized component excites this charge across the gap (ii), with, lastly, the second half cycle of the THz component returning the charge to its original momentum (iii). In this way, charge has been excited at a quasi-momentum $\mathbf{q}$ with conduction-valence energy difference, $\epsilon_c - \epsilon_v$, that is not equal to the circularly polarized light energy $\hbar\omega_{\text{circ}}$ (and hence, not equal to the bandgap to which this light is tuned). To further clarify the roles of the various pulse components, we show in Fig. 2B the dependence of the charge excitation and current on the amplitude of the hencomb pulse components. The circularly polarized pulse component is seen to determine the excited state population, as can be seen from the fact that the hencomb pulse and its circularly polarized component acting alone excite almost the same charge (note that the A_0^2 dependence is consistent with dominance by one-photon processes). In contrast, variation of the amplitude of the THz pulse component results in almost no change in the excited state population but does yield substantial change in the spin current strength through changing the band velocity of the excited charge population (Fig. 2B, inset). To emphasize this symmetry breaking role of the THz light component [see (*24*–*28*) for further applications of the role of symmetry breaking by light in the context of photocurrent generation], we show in Fig. 2C the dependence on the spin current on the THz carrier envelope phase (CEP). As expected, we find a sinusoidal dependence on CEP with the maximal current when THz pulse temporal asymmetry is maximized, i.e., CEPs of $\pi/2$ and $3\pi/2$, while the current falls to zero when the THz component becomes temporally symmetric (CEP of 0 and π).

Valley and spin currents in WSe_2

Evidently, the hencomb pulse has twice the number of parameters as a standard Gaussian envelope laser pulse: We now explore the degree of control of current generation it offers. The response of

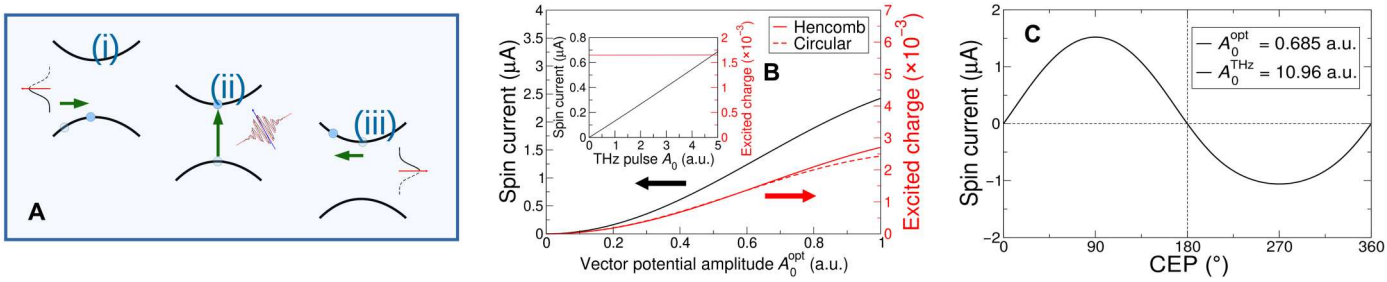

Fig. 2. Exploring the origin of the current control property of the hencomb pulse. (**A**) Schematic illustration of the action of the hencomb pulse: (i) A half cycle of THz light drives an intraband motion sending states distant from the gap edge to the gap edge; (ii) the optical component excites states across the gap; (iii) lastly, the second half cycle of THz light returns the state to its original momentum. The overall action of the hencomb pulse is thus to excite charge at a finite valley momentum determined by the THz pulse polarization vector. (**B**) Dependence of the spin current on the amplitude of the optical (main panel) and the THz components (inset) of the hencomb pulse. Note that a hencomb pulse excites almost exactly the same amount of charge as its corresponding circularly polarized component acting alone (right-hand axis, main panel), showing that it is this latter component that controls the population of the excited state. In contrast, the THz pulse amplitude has almost no effect on the excited state population (right-hand axis, inset). (**C**) Dependence of spin and valley current on the CEP of the THz pulse. As expected, given the symmetry breaking role of the THz light, we find a sinusoidal dependence upon CEP; for ϕ_{CEP} maximizing temporal asymmetry ($\pi/2$ and $3\pi/2$), we find the largest spin current, while for temporal symmetry of the pulse (0 and π), the current vanishes. Pulse parameters are those of Fig. 1 and the maximum values that the peak power density and electric field maximum attain, over all pulses shown, are 2.6×10^{10} W/cm^2 and 4.6 MV/cm, respectively.

WSe_2 to the color of the circularly polarized pulse is presented in Fig. 3A with the charge current (black) and spin current parallel (red) and perpendicular (green) to the polarization vector of the linearly polarized THz pulse. Two distinct steps can be seen, at 2.25 and 2.65 eV, each resulting in a gain by ~5 μA in the charge current. In contrast, at the second step, the spin current falls to zero before, at higher frequencies, reemerging with switched polarization direction. To unveil the microscopic origin of this behavior in Fig. 3 (B to E), we present the momentum space–resolved charge distribution at t = 60 fs, i.e., after the pulse, for four representative frequencies as labeled in Fig. 3A. As may be seen, the circular pulse excites an energy shell of ~0.1 eV where the first step is associated with switching on transitions from the valence band edge and the second with switching on optical transitions from its spin split partner. The spin polarization of the pure valley current thus has a high degree of control through the color of the hencomb pulse.

As the polarization vector of the THz envelope lies in the plane of the 2D material, it can be used to control the direction of the excited valley current. We show this in Fig. 3J where we present the in-plane angle of the valley current, θ_J, versus the angle of the THz polarization vector, θ_T. The equality $\theta_J = \theta_T$ is satisfied exactly only at the symmetry axis of the trigonal warping (*23*) of the band manifold ($2\pi n/6$, n integer); away from these points, a current perpendicular to the THz polarization vector is generated resulting in a deviation of θ_J from the THz polarization vector angle. This has its origin in the noncancelation of Bloch velocities perpendicular to the THz polarization vector since if this vector does not align with one of the trigonal warping symmetry axis, then reflection symmetry about the polarization vector is lost. This is illustrated in the inset of Fig. 3J where we show, along with the constant energy surface displaying trigonal warping, a high-symmetry axis, with evident reflection symmetry, and a low-symmetry axis where this is broken.

The hencomb pulses investigated thus far have precise matching of the centers of the two pulse components, and experimentally, this is unlikely to be perfectly satisfied. In section S2, we show that, even for quite substantial mismatch between the centers of the linearly polarized THz and circularly polarized pulses, the current generation and control properties of the pulse remain robust, although with some reduction in magnitude. Also shown in section S2 are hencomb pulses in which the THz envelope is directly taken from the experiment; the controlled current-generating properties of the hencomb pulse are also found in this case, demonstrating robustness to the noisy and non-monocycle THz waveforms typically found in the experiment. In general, as the pulse parameters of the THz and optical components are experimentally attainable, peak electric fields of 1 to 5 MV/cm at THz frequencies have been reported for ultrafast pulses (*29*–*31*). The laser pulses we use here are within the scope of current experimental capabilities.

Valley current states in bilayer graphene

A long-standing goal in the field of graphene and few-layer graphenes has been to generate a pure valley current. The majority of proposed schemes comprise the design of valley filters, either by using the valley-contrasting gauge field induced by lattice deformation (*32*–*35*) or valley-polarized edge states (*36*); most recently, valley-polarized scattering states from a biased quantum dot in bilayer graphene have been considered (*37*). Here, we show that a hencomb pulse applied to biased bilayer graphene results in a fully controllable and 75 to 85% pure valley-polarized current depending on the value of the gap and the dephasing time.

We consider a minimal tight-binding scheme using only π-bands and use the corresponding time-dependent Schrödinger equation to examine the charge dynamics (technical details of these standard methodologies are provided in Materials and Methods). An interlayer bias opens a gap at the Dirac point, creating a so-called Mexican hat band structure as illustrated in Fig. 4A. This unveils the intrinsic nonzero valley Chern number in bilayer graphene and allows coupling to the valley degree of freedom by circularly polarized light (*38*). As recently shown (*39*), this creates a "ring" of excited charge reflecting the fact that the avoided crossing occurs at the intersection of the two bias shifted cones of each layer —a circle centered at the K point—and the Berry curvature is maximal on this circle.

In Fig. 4C, we show the frequency dependence of the valley and charge currents for hencomb pulses with the THz polarization vector again along a zigzag edge direction (60°). The valley and

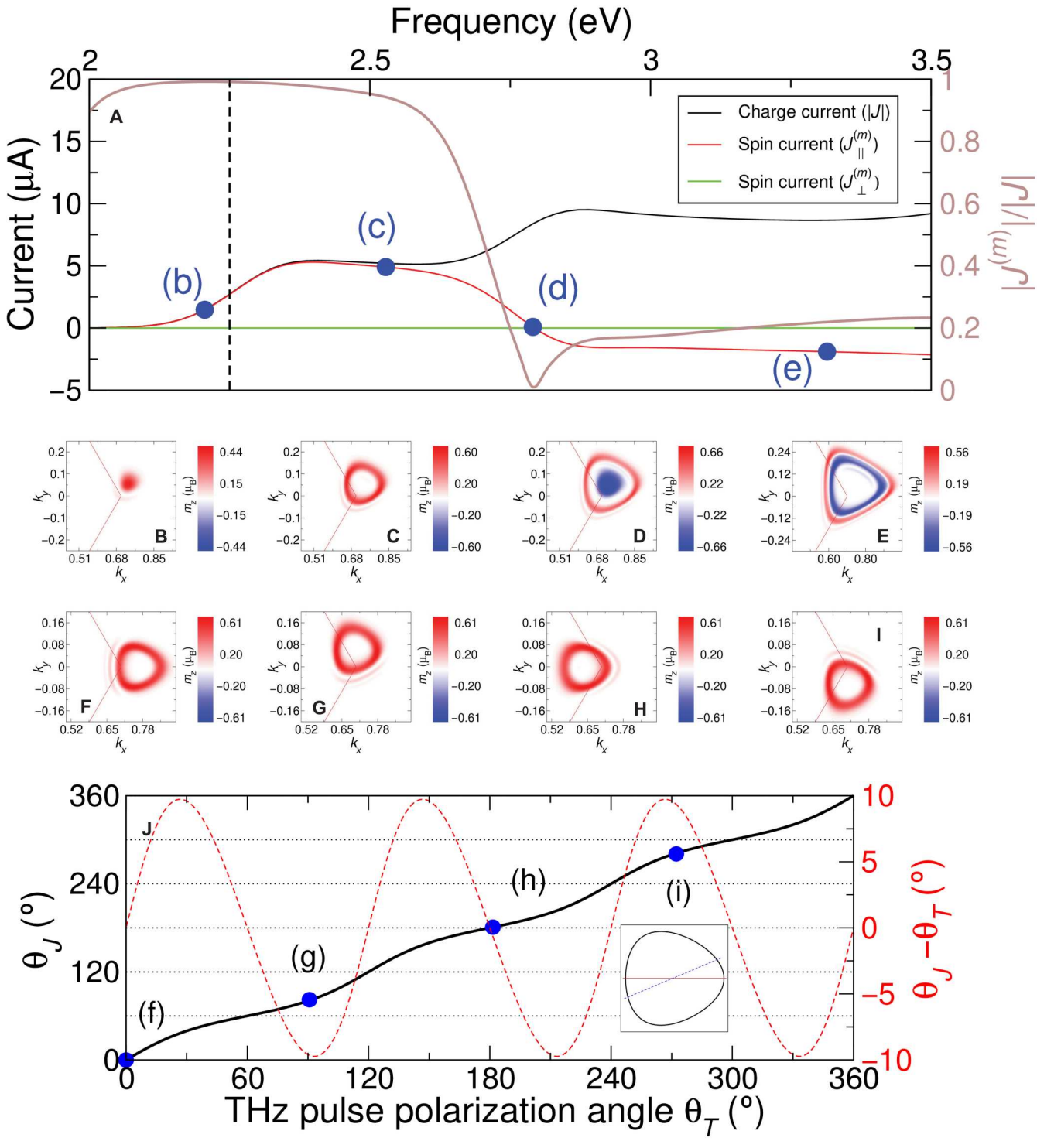

Fig. 3. Control over spin currents by application of a hencomb pulse to WSe_2. (**A**) Varying the frequency of the hencomb pulse generates a rich current response in WSe_2 with steps in the charge and spin current associated with the two spin split band edges. For each of the points labeled in (A), the corresponding momentum-resolved excited charge is shown in (**B**) to (**E**). Two frequency regimes can be identified: single-band excitation (B and C) which generates a nearly pure spin current and larger frequencies which excite from both spin channels resulting, for 2.3 eV, in a switching of the polarization of the spin current. (**F** to **J**) Variation of the angle (θ_T) of the polarization of the THz component of the hencomb pulse controls the direction (θ_J) of the spin/valley current (J). As can be seen in (F) to (I), the excited charge distribution rotates around the *K* point following the polarization vector of the THz light. Note that the angles θ_J and θ_T are equal only when the THz polarization vector coincides with a symmetry axis of the valley trigonal warping (*23*), $\theta_T = n\pi/3$, *n* integer [illustrated in the inset of (J)]. In all cases, the circular (THz) component amplitude is 0.685 a.u. (10.96 a.u.), the FWHM is 16.5 fs for both components, and, in (J), the circular pulse frequency is 2.5 eV. The maximal values attained over all pulses by the peak power density and electric field maximum are 1.9×10^{10} W/cm^2 and 2.2 MV/cm, respectively.

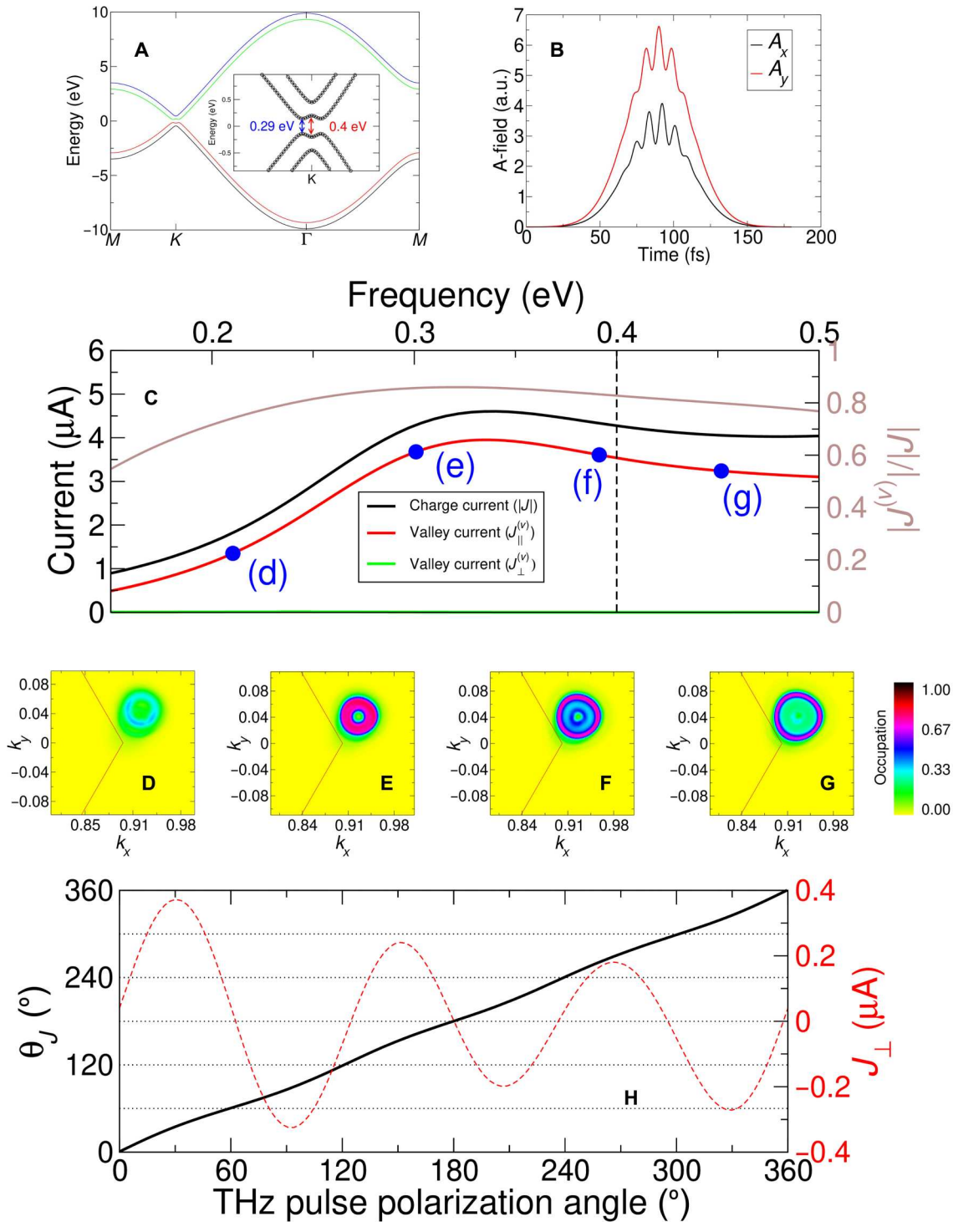

Fig. 4. Valley current in bilayer graphene generated by a hencomb pulse. The band structure and vector potential of the laser pulse are shown in (**A**) and (**B**), respectively. (**C**) Variation of the frequency of the hencomb pulse results in a maximal current signal at frequencies corresponding to transitions across the gap minimum, with the near equality of the valley and charge currents indicating almost complete valley polarization of the current. The corresponding momentum space charge distribution resulting from the hencomb pulse is shown for four representative frequencies in (**D**) to (**G**). Complete control over the direction of the optically induced current is provided by the polarization vector of the THz component, as shown in (**H**). Note that, for the polarization vector displaced from one of the symmetry axis of the valley trigonal warping ($\theta_T = n\pi/3$, n integer), a small current perpendicular $J_\perp$ to the THz polarization vector exists. For the data in (C), the circular/THz component amplitudes are 0.685/6.85 a.u., while in (H), the circular component has an increased amplitude of 1.37 a.u. and a frequency of 0.28 eV. The maximum values attained by the peak power density and peak electric field over all pulses are 2.9×10^8 W/cm^2 and 2.46 MV/cm, respectively.

charge currents are nearly equal, indicating an almost pure valley current, with a maximum in the current response corresponding to the minimum gap of the "brim" of the Mexican hat. The corresponding momentum space–resolved charge excitation (Fig. 4, D to G) reveals that the ring of excited charge is displaced off the valley center, breaking the k_{valley}, $-k_{valley}$ symmetry of the pure circular pulse and resulting in a net valley current. The direction of this current is governed by the THz polarization vector (see Fig. 4J) with the direction of the current vector (θ_J) again only exactly equal to that of the THz polarization vector along symmetry axis of the valley trigonal warping.

Note that, here, we have included decoherence with a dephasing time of 20 fs used. In contrast to WSe_2 in bilayer graphene, decoherence noticeably reduces the valley current polarization—from ~95% purity to ~80% purity for light tuned to the "Mexican hat brim" (the corresponding momentum-resolved excitation is shown in Fig. 4E). The reduction in current due to decoherence arises as charge excitation across the gap is suppressed by dephasing. Furthermore, the importance of decoherence increases as the bilayer graphene gap falls, with gaps of <100 meV showing increasing degradation of the valley current at a dephasing time of 20 fs; see section S1 for further details.

Time-dependent ab initio simulation: WSe_2

Having established the physics of a hencomb pulse using minimal tight-binding models, we now probe how this physics is manifested in state-of-the-art time-dependent density function simulations (*40*–*43*). In Fig. 5, we present the current induced by two hencomb pulses in WSe_2, with the vector potential shown in Fig. 5 (A and B), respectively. These pulses generate a charge excitation displaced from the *K* valley in the k_x direction, with the larger amplitude of the THz envelope of the second pulse creating a correspondingly increased momentum displacement (Fig. 5, E and F).

The current corresponding to this excitation is shown in Fig. 5 (C and D), where we display in the main panels the intraband part of the current and in the insets the total and intraband part for the full simulation time. It turns out that the total current converges very slowly with the size of the **k**-grid due to rapid oscillation in momentum space of the interband current which, however, for sufficiently high **k**-grid, is insignificant in the residual post-pulse current (see the Supplementary Materials). Exactly, the J_x valley current expected on the basis of our model Hamiltonian investigations is observed, and thus, the effect of current control by hybrid hencomb pulses holds also for a realistic (i.e., ab initio) description of femtosecond dynamics.

Finally, one notes that the large THz amplitude pulse (Fig. 5B) generates a weaker current than the weaker THz amplitude pulse (Fig. 5A) with, in addition, a substantial J_y component observed. This arises as, for large THz amplitude, the charge excitation is driven out of the *K* valley and into the vicinity of the *M* point. Here, Bloch velocities are much reduced, resulting in a reduction of the hencomb current due to a reduction in the Bloch velocities of all excited states. The breaking of local C_3 symmetry of the band manifold once the charge excitation leaves the *K* valley also underpins the generation of the J_y component of the current for the large amplitude pulse.

DISCUSSION

Because of its comparable energy to key electronic features such as superconducting gaps and magnetic reorientation energies, THz light is emerging as a key tool in the search for optical control over quantum materials. Here, we have presented an unusual case where THz light is shown to create and control valley current in diverse valley active materials, despite the fact that valley gaps are in the optical range, and so THz light can, by itself, result in no excitation of the electronic system. To achieve this, we have used hybrid hencomb pulses that combine linearly polarized THz light with circularly polarized light tuned to the gap.

This complete control over valley current is underpinned by the dual nature of electronic wave functions: Circularly polarized light couples to the lattice periodic part of the wave function, while THz light couples only through the Bloch envelope that the quantum states in all translationally symmetric materials have; together, this combines interband valley excitation with intraband motion to create unsymmetrical valley distributions that have a finite and controllable current.

We have shown that this effect holds in two contrasting materials, the strong SO dichalcogenide WSe_2 and bilayer graphene. Hencomb pulses will generate controllable valley current in any

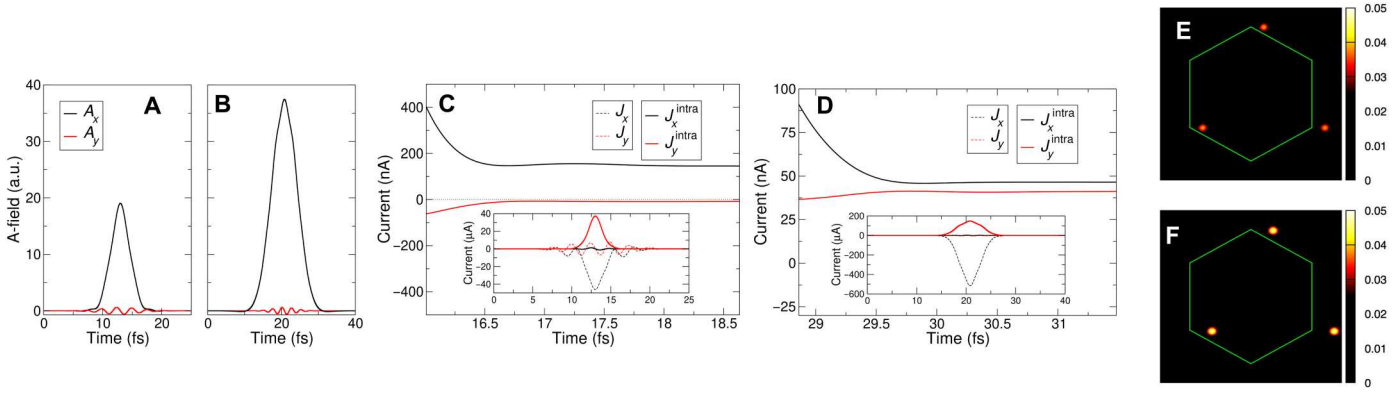

Fig. 5. Hencomb residual current in WSe_2 calculated using TD-DFT. (**A** and **B**) Vector potential with (**C** and **D**) the corresponding valley current. Main panels show the intraband component of the current, while insets show both the intraband current and the total current, which cannot be converged with a computationally feasible **k**-mesh. (**E** and **F**) Momentum-resolved excitation created by pulses in (A) and (B), respectively. For the pulse shown in (A), the fluence is 0.221 mJ/cm^2 with a peak power density of 5.33 × 10^{10} W/cm^2, while the pulse in (B) has a fluence of 0.407 mJ/cm^2 and a peak power density of 5.95 × 10^{10} W/cm^2.

valley active material provided that the THz envelope—which, as it is linearly polarized, cannot valley distinguish—does not itself excite charge. This places the lower gap limit at around 40 meV for a 1-THz guiding envelope, including therefore many topological insulator systems and 2D semi-conductors and magnets. The approach that we describe thus should have wide applicability in a range of valley active materials, opening new avenues for spintronics and valleytronics in 2D systems.

For the situation in which excitons survive screening by excited charge, i.e., for sufficiently weak hencomb pulses, an open question is how the excitonic fraction would differ from that created by a standard circularly polarized pulse. In particular, whether the exciton would inherit the hencomb momentum shift acquired by all single-particle excitations (which would then manifest as an excitonic current). Exploring this requires the consistent treatment of single and composite many body particles in a pumped time-dependent calculation, well beyond the current state of the art in both ab initio and tight-binding theory. The possibility of rich hencomb excitonic physics thus remains a tantalizing question for future work.

MATERIALS AND METHODS

Coherent dynamics

Time evolution proceeds via the Schödinger equation

$$i\partial_t \Psi(t) = H\Psi(t) \tag{1}$$

where $|\Psi(t)\rangle$ is the system key at time t.

This time-dependent system key can be expanded in a basis of Bloch states at crystal momentum $\mathbf{k}(t)$

$$|\Psi_{\mathbf{q}}(t)\rangle = \sum_{\alpha} c_{\alpha\mathbf{q}}(t)\,|\Phi_{\alpha\mathbf{k}(t)}\rangle \tag{2}$$

with $\mathbf{k}(t) = \mathbf{q} - \mathbf{A}(t)/c$ given by the Bloch acceleration theorem (with $\mathbf{q}$ the crystal momentum at $t = 0$). The Bloch states $|\Phi_{\mathbf{k}\alpha}\rangle$ can be expressed (again suppressing nonsite atomic indices) as

$$|\Phi_{\mathbf{k}\alpha}\rangle = \frac{1}{\sqrt{N_n}} \sum_{\mathbf{R}_i} e^{i\mathbf{k}\cdot[\mathbf{R}_i^{(n)} + \mathbf{v}_\alpha^{(n)}]}\,|\mathbf{R}_i + \mathbf{v}_\alpha\rangle \tag{3}$$

where $|\mathbf{R}_i + \mathbf{v}_\alpha\rangle$ is a localized orbital at site $\mathbf{R}_i + \mathbf{v}_\alpha$ with $\mathbf{R}_i$ being a lattice vector and $\mathbf{v}_\alpha$ being the basis vector of sublattice α.

Insertion of a complete set of Bloch states at each time step into Eq. 1 then results in

$$i\partial_t c_{\mathbf{q}} = H_0[\mathbf{k}(t)]c_{\mathbf{q}} \tag{4}$$

the equation of motion for c is the two-vector of expansion coefficients in the basis states at $\mathbf{k}(t)$.

We solve Eq. 4 using the Crank-Nicolson method

$$c_n = \left[1 - \frac{H_0(t_n)\Delta t}{2i}\right]^{-1}\left[1 + \frac{H_0(t_{n-1})\Delta t}{2i}\right]c_{n-1} \tag{5}$$

A k-grid of 50 × 50 to 200 × 200 points in the Brillouin zone is generally used; the principal quantity that we are interested in is the intraband current which (see the Supplementary Materials) is converged already at the smaller grid size. The minimal basis results in good convergence already for time steps of 10 to 30 attoseconds. Note that by unitary transformation, we can express Eq. 4 in a basis of eigenstates at $\mathbf{k}(t)$, $i\partial_t b_{\mathbf{q}} = D[\mathbf{k}(t)]b_{\mathbf{q}}$ with D the matrix of intra- and interband dipole matrix elements. As emphasized in (*44*), the former can be removed by including the Berry phase in the definition of Bloch states.

Density matrix dynamics

We include scattering that induces a loss of coherence (i.e., Einstein–Podolsky–Rosen coupling to the environment) in the simplest possible model

$$\partial_t \rho = -i[H, \rho] + \frac{1}{T_{\mathrm{dco}}}(\rho - \mathrm{Diag}[\rho]) \tag{6}$$

where Diag[ρ] denotes the matrix comprising only the diagonal elements of the density matrix ρ, and T_{dco} is a phenomenological decoherence time. Here, the density matrix is expressed in the eigenbasis at $\mathbf{k}(t)$, and thus, the last term in Eq. 6 encodes the suppression of quantum interference resulting from decoherence.

We use the standard fourth-order Runge-Kutta method for time propagating the density matrix

$$\rho_{n+2} = \rho_n + \Delta t(k_1 + 2k_2 + 2k_3 + k_4)/3 \tag{7}$$

where

$$k_1 = f(t_n, \rho_n) \tag{8}$$

$$k_2 = f(t_{n+1}, \rho_n + \Delta t k_1) \tag{9}$$

$$k_3 = f(t_{n+1}, \rho_n + \Delta t k_2) \tag{10}$$

$$k_4 = f(t_{n+1}, \rho_n + 2\Delta t k_3) \tag{11}$$

where f denotes the right-hand side of the Liouville-von Neumann equation (Eq. 6).

Laser pulse

In all calculations, the laser pulse is described by a series of waveforms with Gaussian envelope form and with pulse center $t_0^{(i)}$

$$\mathbf{A}(t) = \sum_i \mathbf{A}_0^{(i)} \exp\left(-\frac{[t - t_0^{(i)}]^2}{2\sigma_i^2}\right)\cos[\omega_i t + \phi_{\mathrm{cep}}^{(i)}] \tag{12}$$

where $\mathbf{A}_0^{(i)}$ is the pulse amplitude vector, σ_i is related to the full width at half maximum by FWHM $= 2\sqrt{2\ln 2}\sigma_i$, ω_i is the frequency of the light, and $\phi_{\mathrm{cep}}^{(i)}$ is the CEP.

Tight-binding simulation for tungsten dichalcogenide

While a description of the band structure near the K point can be obtained via the $\mathbf{k}\cdot\mathbf{p}$ method, fitting to GW calculations (*45*), for ultrafast laser pulses, one requires a full Brillouin zone interpolation as, depending on the magnitude of the vector potential, one can move arbitrarily far from the high-symmetry K points of the low-energy manifolds. This necessitates a different approach, and here, we take the simplest possible route of taking the gapped graphene Hamiltonian to describe the two low-energy spin manifolds.

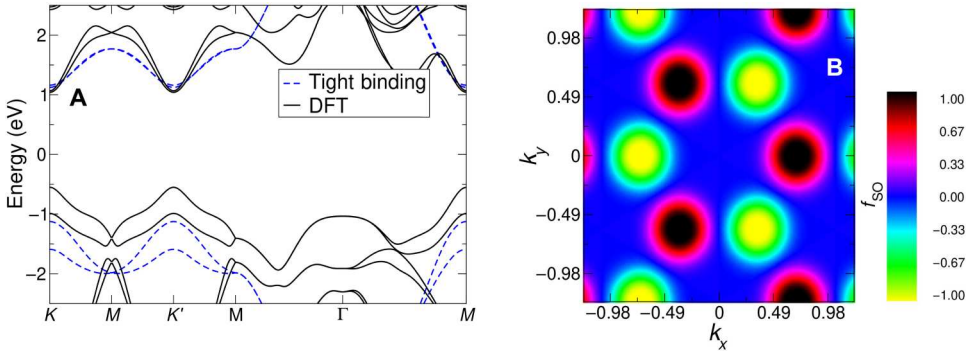

Fig. 6. Model for WSe_2 band structure. (**A**) Band structure of WSe_2 calculated via DFT-LDA, which produces a gap of 1.6 eV, and the model band structure which has the larger gap of 2.25 eV. (**B**) The function $f_{SO}(\mathbf{k})$ used to model the **k** dependence of SO coupling in WSe_2.

This is permissible as, in the low-energy sector, SO coupling is diagonal in pseudo-spin and spin space, being $\lambda_{SO}\sigma_z \otimes \tau_z$ with the σ-matrices describing pseudo and the τ-matrices physical spin space. Including both band and SO-coupling terms then gives for the low-energy Hamiltonian

$$H = \begin{pmatrix} H_\uparrow & 0 \\ 0 & H_\downarrow \end{pmatrix} \tag{13}$$

where

$$H_\sigma = \begin{pmatrix} \Delta & f_{\mathbf{k}} \\ f_{\mathbf{k}}^* & -\Delta \end{pmatrix} + \sigma \begin{pmatrix} \Delta_v^{SO} & 0 \\ 0 & \Delta_c^{SO} \end{pmatrix} f_{SO}(\mathbf{k}) \tag{14}$$

where we have included a different SO splitting for valance and conduction (see Table 1) as in WSe_2 these splittings are markedly different. As the SO splitting is substantial only in the *K* valleys and moreover changes sign at conjugate valleys (required to preserve *T* symmetry), we multiply by a **k**-dependent scale function, $f_{SO}(\mathbf{k})$.

In the above expression (14)

$$f_{\mathbf{k}} = \sum_j t_\perp e^{i\mathbf{k}.\boldsymbol{\nu}_j} \tag{15}$$

where $\boldsymbol{\nu}_j$ represent the nearest-neighbor vectors, and the SO scale function is given by

$$f_{SO}(\mathbf{k}) = \sum_{\mathbf{k}_{MT}} \nu(\mathbf{k}_{MT}) \exp\left[-\frac{1}{2}(|\mathbf{k}| - |\mathbf{k}_{MT}|)^2/\lambda_{SO}^2\right] \tag{16}$$

where $\nu(\mathbf{k}_{MT})$ takes on values of +1 at the *K* valley and −1 and the K^* valley and the sum $\mathbf{k}_{MT}$ is over the union of the translation groups of the two inequivalent *K* and K^* points. The value of λ_{SO} can be found in Table 1 and is chosen so that $f_{SO}(\mathbf{k})$ falls to zero outside the vicinity of the low-energy *K* valleys; a plot of the resulting $f_{SO}(\mathbf{k})$ is shown in Fig. 6B.

Experimental results for the determination of the quasi-particle gap fall in the range of 2.0 to 2.5 eV (*46*, *47*), while GW theory finds quasi-particle gaps in the range of 2.38 to 2.51 eV (*48*, *49*); we take 2.25 eV as the gap—in the middle of this range—although we stress that the precise value of the gap has no qualitative impact on our results. The resulting band structure (with a comparison to that of density functional theory calculation in the local density approximation (DFT-LDA) is shown in Fig. 6A.

Equations 13 to 16 represent the simplest model that can capture (i) the local band structure at *K* and (ii) the switching of the sign of SO coupling at conjugate valleys. We note that Eqs. 13 and 14 represent simply the usual minimal four-band **k**. **p** Hamiltonian, but with the functions $f_{\mathbf{k}}$, Eq. 15, and $f_{SO}(\mathbf{k})$, Eq. 16, interpolating the hopping and SO over the Brillouin zone. This latter function is designed to capture key features of the first-principles band structure, namely, (i) it must limit to the correct SO coupling at the high-symmetry *K* points [met by choosing $\Delta_{v/c}^{SO}$ in Eq. 14 and the condition $f_{SO}(\mathbf{K}) = 1$] and (ii) change sign at conjugate valleys, ensured by $\nu(\mathbf{K}) = -\nu(\mathbf{K}^*)$. Away from the *K* valleys, its interpolation form is arbitrary as our pulses do not access regions of the BZ that fall outside the valleys; we thus take the simplest Gaussian interpolation. Close to the *M* points, this is not therefore guaranteed (or likely) to reproduce the DFT band structure. As can be seen from Fig. 6A while close to the *K* points, the tight-binding (TB) and first-principles band structure are in good agreement, and close to the M points, the TB and first-principles DFT band structures visibly differ in the curvature of the bands.

Table 1. Parameters for calculation of WSe_2 in a minimal four-band model.

Δ	Δ_v^{SO}	Δ_v^{SO}	$t_\perp$	λ_{SO}
2.5 eV	0.466 eV	−0.037 eV	−1.4 eV	0.05

Tight-binding simulation for bilayer graphene

For the extension to bilayer graphene, we employ the standard nearest neighbour model with in-plane hopping −3.2 eV and interlayer hopping 0.4 eV [see e.g., (*37*)].

Supplementary Materials

This PDF file includes:

Sections S1 to S5
Figs. S1 to S13

REFERENCES AND NOTES

1. R. Suzuki, M. Sakano, Y. J. Zhang, R. Akashi, D. Morikawa, A. Harasawa, K. Yaji, K. Kuroda, K. Miyamoto, T. Okuda, K. Ishizaka, R. Arita, Y. Iwasa, Valley-dependent spin polarization in bulk MoS_2 with broken inversion symmetry. *Nat. Nanotechnol.* **9**, 611–617 (2014).
2. K. F. Mak, D. Xiao, J. Shan, Light-valley interactions in 2D semiconductors. *Nat. Photonics* **12**, 451–460 (2018).
3. P. Chen, T. W. Lo, Y. Fan, S. Wang, H. Huang, D. Lei, Chiral coupling of valley excitons and light through photonic spin-orbit interactions. *Adv. Opt. Mater.* **8**, 1901233 (2020).
4. D. Xiao, G.-B. Liu, W. Feng, X. Xu, W. Yao, Coupled spin and valley physics in monolayers of MoS_2 and other group-VI dichalcogenides. *Phys. Rev. Lett.* **108**, 196802 (2012).
5. K. F. Mak, K. He, J. Shan, T. F. Heinz, Control of valley polarization in monolayer MoS_2 by optical helicity. *Nat. Nanotechnol.* **7**, 494–498 (2012).
6. J. Xiao, Z. Ye, Y. Wang, H. Zhu, Y. Wang, X. Zhang, Nonlinear optical selection rule based on valley-exciton locking in monolayer ws_2. *Light Sci. Appl.* **4**, e366 (2015).
7. F. Langer, C. P. Schmid, S. Schlauderer, M. Gmitra, J. Fabian, P. Nagler, C. Schüller, T. Korn, P. G. Hawkins, J. T. Steiner, U. Huttner, S. W. Koch, M. Kira, R. Huber, Lightwave valleytronics in a monolayer of tungsten diselenide. *Nature* **557**, 76–80 (2018).
8. G. Berghäuser, I. Bernal-Villamil, R. Schmidt, R. Schneider, I. Niehues, P. Erhart, S. M. de Vasconcellos, R. Bratschitsch, A. Knorr, E. Malic, Inverted valley polarization in optically excited transition metal dichalcogenides. *Nat. Commun.* **9**, 971 (2018).
9. S. Ishii, N. Yokoshi, H. Ishihara, Optical selection rule of monolayer transition metal dichalcogenide by an optical vortex. *J. Phys. Conf. Ser.* **1220**, 012056 (2019).
10. R. E. F. Silva, M. Ivanov, Á. Jiménez-Galán, All-optical valley switch and clock of electronic dephasing. *Opt. Express* **30**, 30347–30355 (2022).
11. S. Sharma, P. Elliott, S. Shallcross, Valley control by linearly polarized laser pulses: Example of WSe_2. *Optica* **9**, 947–952 (2022).
12. J. R. Schaibley, H. Yu, G. Clark, P. Rivera, J. S. Ross, K. L. Seyler, W. Yao, X. Xu, Valleytronics in 2D materials. *Nat. Rev. Mater.* **1**, 16055 (2016).
13. W.-Y. Shan, J. Zhou, D. Xiao, Optical generation and detection of pure valley current in monolayer transition-metal dichalcogenides. *Phys. Rev. B* **91**, 035402 (2015).
14. R. Asgari, D. Culcer, Unidirectional valley-contrasting photocurrent in strained transition metal dichalcogenide monolayers. *Phys. Rev. B* **105**, 195418 (2022).
15. H. Yuan, X. Wang, B. Lian, H. Zhang, X. Fang, B. Shen, G. Xu, Y. Xu, S.-C. Zhang, H. Y. Hwang, Y. Cui, Generation and electric control of spin–valley-coupled circular photogalvanic current in WSe2. *Nat. Nanotechnol.* **9**, 851–857 (2014).
16. C. Jin, J. Kim, M. I. B. Utama, E. C. Regan, H. Kleemann, H. Cai, Y. Shen, M. J. Shinner, A. Sengupta, K. Watanabe, T. Taniguchi, S. Tongay, A. Zettl, F. Wang, Imaging of pure spin-valley diffusion current in WS_2-WSe_2 heterostructures. *Science* **360**, 893–896 (2018).
17. T. Y. T. Hung, K. Y. Camsari, S. Zhang, P. Upadhyaya, Z. Chen, Direct observation of valley-coupled topological current in MoS2. *Sci. Adv.* **5**, eaau6478 (2019).
18. A. Bera, S. Bera, S. Kalimuddin, S. Gayen, M. Kundu, B. Das, M. Mondal, Review of recent progress on THz spectroscopy of quantum materials: Superconductors, magnetic and topological materials. *Eur. Phys. J. Spec. Top.* **230**, 4113–4139 (2021).
19. E. A. Mashkovich, K. A. Grishunin, R. M. Dubrovin, A. K. Zvezdin, R. V. Pisarev, A. V. Kimel, Terahertz light–driven coupling of antiferromagnetic spins to lattice. *Science* **374**, 1608–1611 (2021).
20. P. Khan, M. Kanamaru, K. Matsumoto, T. Ito, T. Satoh, Ultrafast light-driven simultaneous excitation of coherent terahertz magnons and phonons in multiferroic BiFe O_3. *Phys. Rev. B* **101**, 134413 (2020).
21. A. L. Chekhov, Y. Behovits, J. J. F. Heitz, C. Denker, D. A. Reiss, M. Wolf, M. Weinelt, P. W. Brouwer, M. Münzenberg, T. Kampfrath, Ultrafast demagnetization of iron induced by optical versus terahertz pulses. *Phys. Rev. X* **11**, 041055 (2021).
22. S. Shallcross, Q. Z. Li, J. K. Dewhurst, S. Sharma, P. Elliott, Ultrafast optical control over spin and momentum in solids. *Appl. Phys. Lett.* **120**, 032403 (2022).
23. A. Säynätjoki, L. Karvonen, H. Rostami, A. Autere, S. Mehravar, A. Lombardo, R. A. Norwood, T. Hasan, N. Peyghambarian, H. Lipsanen, K. Kieu, A. C. Ferrari, M. Polini, Z. Sun, Ultra-strong nonlinear optical processes and trigonal warping in MoS_2 layers. *Nat. Commun.* **8**, 893 (2017).
24. T. Boolakee, C. Heide, A. Garzón-Ramírez, H. B. Weber, I. Franco, P. Hommelhoff, Light-field control of real and virtual charge carriers. *Nature* **605**, 251–255 (2022).
25. T. Higuchi, C. Heide, K. Ullmann, H. B. Weber, P. Hommelhoff, Light-field-driven currents in graphene. *Nature* **550**, 224–228 (2017).
26. L. Chen, Y. Zhang, G. Chen, I. Franco, Stark control of electrons along nanojunctions. *Nat. Commun.* **9**, 2070 (2018).
27. A. Schiffrin, T. Paasch-Colberg, N. Karpowicz, V. Apalkov, D. Gerster, S. Mühlbrandt, M. Korbman, J. Reichert, M. Schultze, S. Holzner, J. V. Barth, R. Kienberger, R. Ernstorfer, V. S. Yakovlev, M. I. Stockman, F. Krausz, Optical-field-induced current in dielectrics. *Nature* **493**, 70–74 (2013).
28. I. Franco, M. Shapiro, P. Brumer, Robust ultrafast currents in molecular wires through stark shifts. *Phys. Rev. Lett.* **99**, 126802 (2007).
29. J. A. Fülöp, S. Tzortzakis, T. Kampfrath, Laser-driven strong-field terahertz sources. *Adv. Opt. Mater.* **8**, 1900681 (2020).
30. A. D. Koulouklidis, C. Gollner, V. Shumakova, V. Y. Fedorov, A. Pugžlys, A. Baltuška, S. Tzortzakis, Observation of extremely efficient terahertz generation from mid-infrared two-color laser filaments. *Nat. Commun.* **11**, 292 (2020).
31. G. Rodriguez, G. L. Dakovski, Scaling behavior of ultrafast two-color terahertz generation in plasma gas targets: Energy and pressure dependence. *Opt. Express* **18**, 15130–15143 (2010).
32. R. Gupta, F. Rost, M. Fleischmann, S. Sharma, S. Shallcross, Straintronics beyond homogeneous deformation. *Phys. Rev. B* **99**, 125407 (2019).
33. M. Settnes, S. R. Power, M. Brandbyge, A.-P. Jauho, Graphene nanobubbles as valley filters and beam splitters. *Phys. Rev. Lett.* **117**, 276801 (2016).
34. L.-Y. Zhao, H. Wang, H.-Y. Wang, Q. Zhou, X.-L. Zhang, T. Cui, L. Wang, T.-Y. Liu, Y.-X. Han, Y. Luo, Y.-Y. Yue, M.-S. Song, H.-B. Sun, Ultrafast modulation of valley dynamics in multiple WS_2-Ag gratings strong coupling system. *PhotoniX* **3**, 5 (2022).
35. Z. Yang, S. Aghaeimeibodi, E. Waks, Chiral light-matter interactions using spin-valley states in transition metal dichalcogenides. *Opt. Express* **27**, 21367–21379 (2019).
36. M. Luo, Z. Li, Optical excitation of valley and spin currents of chiral edge states in graphene with Rashba spin-orbital coupling. *Phys. Rev. B* **96**, 165424 (2017).
37. F. Solomon, S. R. Power, Valley current generation using biased bilayer graphene dots. *Phys. Rev. B* **103**, 235435 (2021).
38. J. Yin, C. Tan, D. Barcons-Ruiz, I. Torre, K. Watanabe, T. Taniguchi, J. C. W. Song, J. Hone, F. H. L. Koppens, Tunable and giant valley-selective Hall effect in gapped bilayer graphene. *Science* **375**, 1398–1402 (2022).
39. A. Friedlan, M. M. Dignam, Valley polarization in biased bilayer graphene using circularly polarized light. *Phys. Rev. B* **103**, 075414 (2021).
40. E. Runge, E. Gross, Density-functional theory for time-dependent systems. *Phys. Rev. Lett.* **52**, 997 (1984).
41. C. A. Ullrich, *Time-Dependent Density-Functional Theory* (Oxford Univ. Press, 2014).
42. P. Elliott, F. Furche, K. Burke, *Excited States from Time-Dependent Density Functional Theory* (John Wiley & Sons, Ltd, 2009), chap. 3, pp. 91–165.
43. S. Sharma, J. K. Dewhurst, E. K. U. Gross, *First Principles Approaches to Spectroscopic Properties of Complex Materials* (Springer Berlin Heidelberg, 2014), pp. 235–257.
44. P. Kumar, T. M. Herath, V. Apalkov, M. I. Stockman, Bilayer graphene in strong ultrafast laser fields. arXiv:2004.09732 [cond-mat] (2020).
45. A. Kormányos, G. Burkard, M. Gmitra, J. Fabian, V. Zólyomi, N. D. Drummond, V. Fal'ko, k.p theory for two-dimensional transition metal dichalcogenide semiconductors. *2D Mater.* **2**, 022001 (2015).
46. M.-H. Chiu, C. Zhang, H.-W. Shiu, C.-P. Chuu, C.-H. Chen, C.-Y. S. Chang, C.-H. Chen, M.-Y. Chou, C.-K. Shih, L.-J. Li, Determination of band alignment in the single-layer MoS2/WSe2 heterojunction. *Nat. Commun.* **6**, 7666 (2015).
47. C. Zhang, Y. Chen, A. Johnson, M.-Y. Li, L.-J. Li, P. C. Mende, R. M. Feenstra, C.-K. Shih, Probing critical point energies of transition metal dichalcogenides: Surprising indirect gap of single layer WSe2. *Nano Lett.* **15**, 6494–6500 (2015).
48. Y. Ding, Y. Wang, J. Ni, L. Shi, S. Shi, W. Tang, First principles study of structural, vibrational and electronic properties of graphene-like MX2 (M=Mo, Nb, W, Ta; X=S, Se, Te) monolayers. *Phys. B: Condens. Matter.* **406**, 2254–2260 (2011).
49. Y. Liang, S. Huang, R. Soklaski, L. Yang, Quasiparticle band-edge energy and band offsets of monolayer of molybdenum and tungsten chalcogenides. *Appl. Phys. Lett.* **103**, 042106 (2013).

Acknowledgments: We acknowledge the North-German Supercomputing Alliance (HLRN) for providing HPC resources that have contributed to the research results reported in this paper. **Funding:** This work was supported by the DFG. S.Shar. would like to thank DFG for funding through project ID 328545488 TRR227 (projects A04). S.Shal. would like to thank DFG for funding through SPP 1840 QUTIF grant no. SH 498/3-1, while P.E. thanks DFG for funding through project 2059421. **Author contributions:** S.Shal. designed the project, performed the calculations and main analysis, and wrote the first draft of the manuscript. P.E. performed the TD-DFT calculations. All authors contributed critically to the analysis and writing of the manuscript. **Competing interests:** The authors declare that they have no competing interests. **Data and materials availability:** All data needed to evaluate the conclusions in the paper are present in the paper and/or the Supplementary Materials.

Submitted 17 October 2022
Accepted 9 February 2023
Published 15 March 2023
10.1126/sciadv.adf3673